AGU ADVANCING EARTH AND SPACE SCIENCE

JGR Space Physics

RESEARCH ARTICLE

10.1029/2021JA029440

Key Points:

- Perpendicular anisotropy of electrons with energies more than 10 keV is responsible for whistler waves generation during dipolarizations
- Whistler waves play an important role in energy exchange between different parts of electron spectrum in energy range more than 2 keV
- Electrons with energies 10–20 keV can be scattered into the loss cone due to their interaction with the low-frequency whistler waves

Supporting Information:

Supporting Information may be found in the online version of this article.

Correspondence to:

A. Y. Malykhin,
anmaurdreg@gmail.com

Citation:

Malykhin, A. Y., Grigorenko, E. E., Shklyar, D. R., Panov, E. V., Le Contel, O., Avanov, L., & Giles, B. (2021). Characteristics of resonant electrons interacting with whistler waves in the nearest dipolarizing magnetotail. *Journal of Geophysical Research: Space Physics*, *126*, e2021JA029440. https://doi.org/10.1029/2021JA029440

Received 12 APR 2021
Accepted 21 JUN 2021

Characteristics of Resonant Electrons Interacting With Whistler Waves in the Nearest Dipolarizing Magnetotail

A. Y. Malykhin[1], E. E. Grigorenko[1], D. R. Shklyar[1], E. V. Panov[2], O. Le Contel[3], L. Avanov[4], and B. Giles[4]

[1]Space Research Institute of Russian Academy of Science, Moscow, Russia, [2]Institute of Physics, Karl-Franz University, Graz, Austria, [3]Laboratoire de Physique des Plasmas, CNRS, Ecole Polytechnique, Sorbonne Université, Université Paris-Saclay, Observatoire de Paris, Paris, France, [4]NASA Goddard Space Flight Center, Greenbelt, MD, USA

Abstract The Magnetospheric Multiscale spacecraft observations in the burst mode allow the determination of the characteristics of resonant electrons interacting with quasi-parallel whistler waves during prolonged dipolarizations in the near Earth magnetotail at $-22\ R_E < X \leq -8\ R_E$. We have detected 163 whistler bursts observed during 48 dipolarization events. The bursts were registered within ∼13 min following the dipolarization onset when the burst mode observations were available. In the majority of events, electrons with energies $W_{res} \geq 10$ keV and pitch angles $\alpha_{res} \sim 100°–130°$ and $\alpha_{res} \sim 50°–80°$made the maximum positive contribution to the growth rate of whistler waves propagating quasi-parallel and antiparallel to the ambient magnetic field, respectively. Our analysis shows that electrons with $W_{res} \sim 10–20$ keV could potentially be scattered into the loss cone by the low frequency whistler waves with $f_w \sim (0.05–0.2)f_{ce}$ (f_w is the wave frequency and f_{ce} is the electron gyrofrequency). The electrons that are scattered into the loss cone can contribute to electron precipitation within ∼13 min following the dipolarization onset. We suggest that whistler waves that are excited due to cyclotron instability driven by the temperature anisotropy of suprathermal electrons (≥2 keV) may, in turn, affect electron distribution in this energy range. Specifically, lower energy resonant electrons transfer a part of their kinetic energy to waves, while more energetic electrons absorb wave energy increasing their kinetic energy. This may lead to the transformation of higher-energy part of electron distribution from Maxwellian to the power law shape.

Plain Language Summary Magnetic dipolarization is an important process in the magnetotail dynamics which manifests in transformation of initially stretched tail-like configuration into the dipole-like configuration. The dipolarization is followed by various processes of energy dissipation and transformation including plasma heating and acceleration as well as generation of different wave modes. In collisionless plasma, wave-particle interactions play a key role in energy exchange between different populations of plasma particles. Also particle interactions with waves may cause particle scattering into the loss cone and their precipitation in the auroral region. The processes of wave-particle interactions usually occur at very short time scales, and their investigation "in situ" requires observations with high time resolution. In this study, we use the Magnetospheric Multiscale spacecraft observations in burst mode and determine the characteristics of resonant electrons interacting with quasi-parallel whistler waves at time scales of the order of a few seconds. We have found that quasi-parallel whistler waves can be generated in the course of dipolarization due to cyclotron instability driven by the temperature anisotropy of suprathermal electrons (≥2 keV). Once have been generated, these waves, in turn, affect electron distribution in this energy range. Specifically, lower energy resonant electrons transfer a part of their kinetic energy to waves, while more energetic electrons absorb wave energy increasing their kinetic energy. We also found that some fraction of suprathermal electrons can be potentially scattered into the loss cone by the low-frequency whistler waves. Such electrons can contribute to electron precipitation within ∼13 min following the dipolarization onset.

1. Introduction

Magnetic dipolarization manifests itself in a sudden increase in the northward component of the magnetic field (B_Z) in the initially stretched magnetic configuration of the Earth's magnetotail. Dipolarizations occur at various time scales, and they are one of the important processes in the magnetotail dynamics, which is often associated with an increase in geomagnetic activity (e.g., Baumjohann et al., 1999; Birn et al., 2019; Sergeev et al., 2012, and references therein).

The origin of prolonged dipolarizations in the near-Earth magnetotail is still under discussion. They can be caused by magnetic flux pileups in the magnetotail transition region (at $X \sim -10$ to -20 R_E) where the stretched magnetotail configuration transforms to a more dipole-like form, and high-velocity bulk flows are braking and rebounding (e.g., Merkin et al., 2019; Nakamura et al., 2009; Panov, Baumjohann, Nakamura, Pritchett, et al., 2019a; Pritchett, 2015; Shiokawa et al., 2005; Takada et al., 2006). Other possible underlying conditions for prolonged dipolarizations can be local disruptions of the Current Sheet (CS) (e.g., McPherron et al., 1973; Miura et al., 1989; Roux et al., 1991) driven by cross-tail current instability (e.g., Lui, 1996, 2011) or other plasma instabilities (Lui, 2004), in particular, the ballooning/interchange instability (e.g., Birn et al., 2018; Merkin & Sitnov, 2016; Panov, Baumjohann, Nakamura, Weygand, et al., 2019b; Panov et al., 2020; Pritchett & Coroniti, 2011; Pritchett et al., 2014).

Once has been generated, the magnetic dipolarization can last from several minutes to several hours (e.g., Sergeev et al., 2012) showing a complicated multiscale spatial structure (e.g., Grigorenko et al., 2016, 2018; Malykhin, Grigorenko, Kronberg, Koleva, et al., 2018; Nakamura et al., 2009). Usually, dipolarization events comprise a prolonged growth of the B_Z field, lasting from a few minutes to tens of minutes, along with multiple short (~1–2 min) B_Z pulses. The B_Z pulses are more frequently observed just after the onset of dipolarization and within the first 10 min after the onset, that is, during the dipolarization growth (e.g., Grigorenko et al., 2016). It has also been shown that strong magnetic field gradients lasting ≤2 s are observed at spatial scales of the order of a few λ_e (λ_e is a local electron inertial length) during the dipolarization growth (Grigorenko et al., 2018). These nonlinear magnetic structures are associated with intense and localized electric currents characterized by the current density up to hundred(s) nA/m^2 (e.g., Nakamura et al., 2018). Such electron-scale electric currents can represent small-scale elements of 3D field-aligned current system forming a substorm current wedge. These findings highlight the importance of electron scale processes in the dynamics of plasma and fields in the near-Earth magnetotail.

The prolonged dipolarizations play an important part in many key processes in the near-Earth tail such as energy transformation and plasma particle heating and acceleration (e.g., Grigorenko et al., 2016; Malykhin, Grigorenko, Kronberg, & Daly, 2018; Malykhin et al., 2019; Malykhin, Grigorenko, Kronberg, Koleva, et al., 2018). While ions are accelerated mainly due to nonadiabatic mechanisms (e.g., Delcourt, 2002; Delcourt & Sauvaud, 1994; Malykhin et al., 2019; Nosé et al., 2000), electrons experience adiabatic betatron and/or Fermi acceleration (e.g., Fu et al., 2011; Smets et al., 1999). It is believed that betatron acceleration of electrons in a gradually growing B_Z field, as well as during B_Z pulses, is responsible for the appearance of perpendicular temperature anisotropy ($T_\perp / T_\parallel > 1$) in electron distributions (e.g., Birn et al., 2014; Fu et al., 2012; Gabrielse et al., 2016; Khotyaintsev et al., 2011), while the parallel anisotropy ($T_\perp / T_\parallel < 1$) could be caused by Fermi acceleration during the shortening of magnetic flux tubes in the course of dipolarization (e.g., Fu et al., 2011; Wu et al., 2006).

The anisotropy of electron velocity distribution function can lead to generation of various types of electromagnetic waves observed during the prolonged dipolarizations, in particular, kinetic Alfvén waves and whistler mode waves (Breuillard et al., 2016; Fu et al., 2014; Grigorenko et al., 2016, 2020; Gurnett et al., 1976; Khotyaintsev et al., 2011; Le Contel et al., 2009; Sagdeev & Shafranov, 1961; Tenerani et al., 2013; Viberg et al., 2014; Zhang & Angelopoulos, 2014; Zhang et al., 1999). Once have been generated, these waves propagate from their source and interact with local electron population modifying its velocity distribution function. The processes of wave-electron interactions, which assume the energy exchange between waves and resonant electrons, affect the local electron anisotropy, as well as lead to electron scattering into the loss cone (e.g., Grigorenko et al., 2020; Shklyar, 2011, 2017; Zhang et al., 2019). The self-consistent dynamics of electron velocity distribution caused by wave-particle interactions may affect the electron currents and small-scale magnetic structures in the dipolarization region, while the scattering of resonant electrons into the loss cone may contribute to auroral electron precipitation during the prolonged dipolarizations. Thus, it is important to determine the characteristics of resonant electrons capable of taking part in the processes of wave-particle interactions during the dipolarization events.

In this paper, we aimed at determining the characteristics of resonant electrons interacting with quasi-parallel whistler waves during the prolonged dipolarizations in the near-Earth magnetotail. The observed bursts of whistler waves have very short durations (a few seconds or less), so that to determine the characteristics of resonant electrons the high time resolution of 3D electron velocity distribution function is required. The Fast Plasma Investigation (FPI) on board MMS probes provides such observations with 30 ms resolution in the burst mode that gives a unique opportunity to investigate this problem. Using these data, Grigorenko et al. (2020) studied the dynamics of anisotropy of electron velocity distribution function associated with bursts of quasi-parallel whistler waves observed in the propagating single Dipolarization Fronts (DFs) at $-25\ R_E \leq X \leq -17\ R_E$. In the present paper, we apply a similar analysis to determine the properties of resonant electrons interacting with quasi-parallel whistler waves in another class of magnetotail phenomena, that is, in the prolonged magnetic dipolarizations, which have more complicated magnetic structure, longer durations, and are usually observed closer to the Earth than the single propagating DFs.

We revealed that during the prolonged dipolarizations in the near-Earth magnetotail (at $-22\ R_E < X \leq -8\ R_E$) the resonant electrons making positive contribution to the growth rate of whistler waves have statistically larger energies (≥10 keV) than the resonant electrons interacting with the whistler waves in single DFs further down the tail. We also found that some fraction of these energetic electrons can be potentially scattered into the loss cone within ~13 min following the dipolarization onset. The structure of the paper is as follows. In Section 2, we present an example of quasi-parallel whistler wave observations during the prolonged dipolarization and analyze the characteristics of resonant electrons interacting with the observed waves. Statistical characteristics of dipolarization events obtained from the analysis of all cases in our data base are presented in Section 3. Section 4 is devoted to the discussion of obtained results.

2. MMS Observations of Quasi-Parallel Whistler Bursts During Prolonged Dipolarization in the Magnetotail

For the analysis, we use the burst mode observations providing by the MMS mission (Burch et al., 2016). 3D electron velocity distribution functions were obtained from FPI (Pollock et al., 2016) with 30 ms time resolution in the energy range from ~10 eV to 30 keV. The magnetic field data and wave observations were obtained from fluxgate magnetometer (FGM) (Russell et al., 2016) and search coil magnetometer (SCM) (Le Contel et al., 2016).

We were looking for the prolonged dipolarization events in the near-Earth Plasma Sheet (PS) at $-22\ R_E < X \leq -8\ R_E$ ($10\ R_E < R \leq 22\ R_E$) and $|Y_{GSM}| \leq 10\ R_E$ during the MMS magnetotail season from May to October 2017. We selected the prolonged magnetic dipolarizations (with duration >4 min) during which the amplitude of the B_Z increase was larger than 5 nT. The geocentric solar magnetospheric (GSM) coordinate system is used everywhere in the paper.

2.1. An Example of a Prolonged Dipolarization and Associated Whistler Bursts Observed on June 2, 2017 Between 10:01:30 and 10:11:30 UT

On June 2, 2017 at 10:01:30–10:11:30 UT, MMS spacecraft were in the near-Earth magnetotail at [−17, −5.5, 2] R_E and observed a prolonged dipolarization in the PS. In Figure 1, we present only MMS-1 observations during this time interval, since the observations from other probes are quite similar. The increase in the B_z field from the background level up to ~18 nT started at ~10:03:30 UT. We refer to this time as "dipolarization onset".

The onset is preceded by a negative B_Z variation, the so-called magnetic dip (e.g., Ohtani et al., 2004; Shiokawa et al., 2005) (see Figure 1a). After the onset, the B_Z field experiences strong fluctuations with multiple B_Z pulses of various amplitudes and durations until ~10:06:30 UT, when the amplitude of the B_Z variations has decreased, but the average value of the B_Z is still large: ~8 nT, and it decreases almost to the background level only at the end of the interval of interest. During the dipolarization, several increases in ion V_X velocity up to ~800 km/s are observed (see Figure 1b). They denote the arrival of the earthward moving BBFs. Ion density drops (see Figure 1c) and the temperature increases (not shown) at the onset of dipolarization indicating that the onset-related DF separates hot and tenuous plasma from a more dense and colder ambient PS population (e.g., Runov et al., 2011; Schmid et al., 2015; Sergeev et al., 2012).

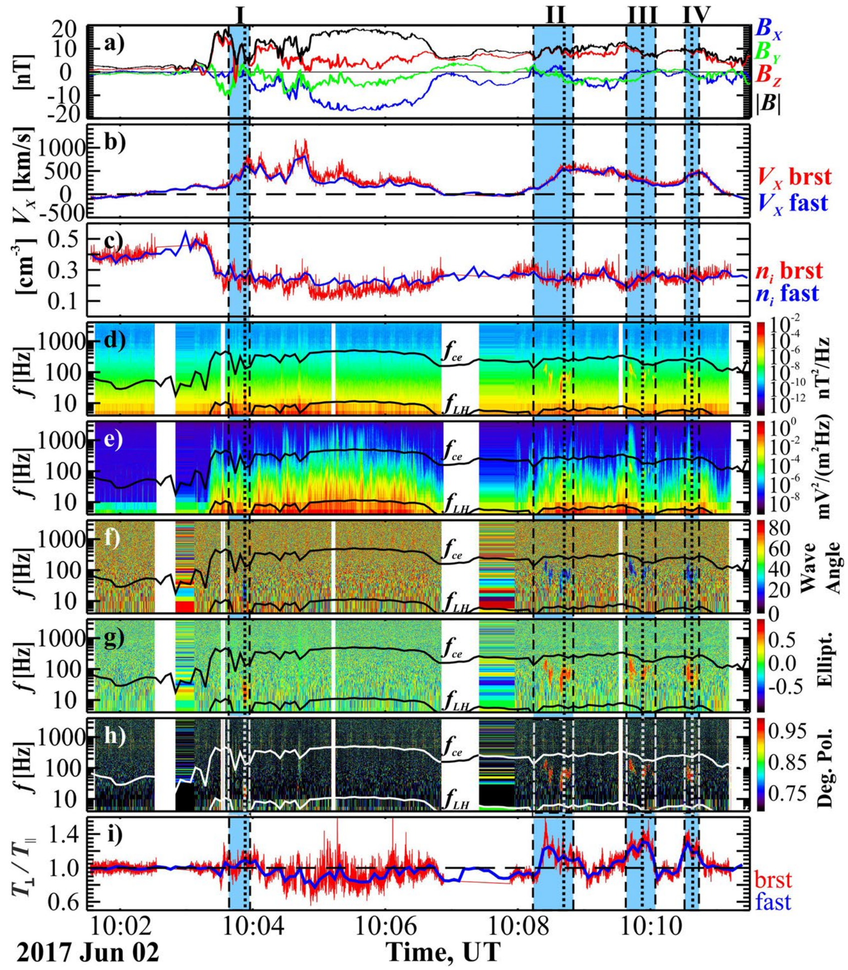

Figure 1. Multicomponent analysis of the prolonged dipolarization event observed by MMS-1 on June 2, 2017. Shown in the figure are (a) three components of the magnetic field and its magnitude |**B**|; (b) V_X component of ion bulk velocity; (c) electron density; (d) power spectral density of the magnetic field fluctuations on (T–F)-plane; (e) the same for the wave electric field; (f) T–F spectrograms of the wave normal angle; (g) ellipticity; (h) the degree of polarization; and (i) electron temperature anisotropy $T_\perp$ / $T_\parallel$. Blue shaded regions confined by the vertical dashed lines mark the intervals of whistler bursts (numbered by "I–IV"). Solid black/white lines in panels (d–h) display the time profiles of the local f_{ce} and f_{LH} (f_{LH} is the lower hybrid resonance frequency).

During the dipolarization, several bursts of whistler waves were observed (see Figures 1d and 1e). These intervals are marked by the dashed vertical lines and shaded in blue in Figure 1. It is worth noting that wave activity was observed also outside the selected intervals. However, we aim at analyzing only waves with small wave normal angles (<40°), which are characterized by right-hand, almost circular polarization (the ellipticity is larger than 0.5 and the degree of polarization >0.7). These wave characteristics are typical of quasi-plane, narrow-banded whistler-mode waves propagating at small angles to the ambient magnetic field. Since multicomponent measurements make it possible to determine all of these quantities, we use all of them to select quasi-parallel whistler bursts for further analysis. These characteristics are consistent with direct determination of the wave normal angle from three component measurements of the magnetic field fluctuations, which show that in most cases the wave normal angle is less than 20° (e.g., Grigorenko et al., 2020; Huang et al., 2012; Le Contel et al., 2009).

The duration of whistler bursts varies from ~0.5 to ~8 s. The first burst was observed within 1 min after the onset during the B_Z pulse (the interval "I" in Figure 1). The other bursts were detected at the later stage of the dipolarization when the B_Z field was quasi-steady but still large (intervals "II–IV"). For Fourier analysis, we used SCM data in the frequency range from 4 to 4,096 Hz with time resolution 0.25 s (sampling frequency

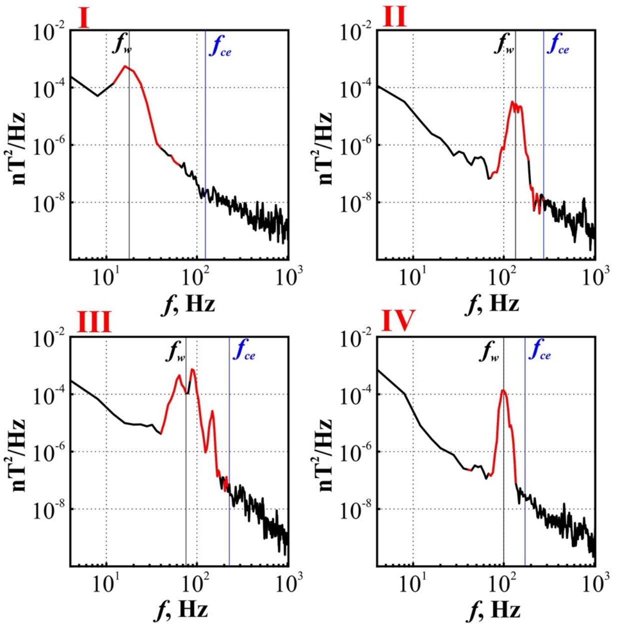

Figure 2. Power spectral density of magnetic fluctuations as functions of frequency at the moments marked by vertical dotted lines within whistler burst intervals "I–IV" shown in Figure 1. The f_{ce} and the frequency of the narrowband quasi-parallel whistler wave, f_w, are marked by the blue and black vertical lines respectively.

was 8,192 Hz). To determine the direction of the ambient magnetic field, we used FGM data in burst mode (128 Hz). The wave polarization was calculated using the method described in, for example, Means (1972) and Samson and Olson (1980).

Figure 2 displays frequency spectra of the power spectral density of the magnetic field fluctuations observed at the moments marked by dotted vertical lines (see Figure 1) within four whistler bursts intervals ("I–IV"). In Figure 2, the frequency spectra are shown by black lines, while the red lines denote the spectra segments for which the wave normal angle was <40° and the degree of polarization was >0.7 peculiar to the quasi-parallel whistler waves discussed above. The "red segments" represent the bulges in the frequency spectra both of the magnetic and electric field (not shown) fluctuations, and they are observed in a finite range of frequencies between local proton plasma frequency and electron gyrofrequency (f_{ce}). The peak frequency (f_w) of these narrowband whistler waves is $f_w \sim 0.1 f_{ce}$, $0.46 f_{ce}$, $0.35 f_{ce}$, and $0.55 f_{ce}$ for the burst intervals "I", "II", "III", and "IV", respectively.

During the dipolarization, strong fluctuations of electron temperature anisotropy $T_\perp / T_\parallel$ are observed (see Figure 1i). It is seen that the bursts of whistler waves are associated with the increases in electron perpendicular anisotropy ($T_\perp / T_\parallel > 1.0$). In the next section, we consider in detail the link between the whistler bursts and $T_\perp / T_\parallel$ variations.

2.2. The Dynamics of Electron Anisotropy Associated With the Whistler Bursts

Figure 3 displays the dynamics of electron flux and temperature anisotropy observed during four intervals of whistler bursts (shown in Figure 1) in four corresponding blocks of panels ("I–IV"). The time profiles of the B_Z field, frequency–time (F–T) spectrogram of the magnetic field fluctuations, and the wave normal angle observed in each interval of the whistler bursts are shown for the reference in panels (a–c) of each block, respectively. We see that the wave normal angle determined from the wave magnetic field measurements is quite small, suggesting quasi-parallel or antiparallel propagation. Although for oblique propagation all cyclotron resonances, including Landau resonance, come into play (e.g., Shklyar & Matsumoto, 2009), for quasi-parallel propagation the first cyclotron resonance remains the most important. Taking this into account, we will limit ourselves to purely parallel or antiparallel propagation when only the first cyclotron resonance remains in effect.

For parallel propagating whistler waves, the parallel energy of resonant electrons ($W_{\|\text{res}}$) can be calculated by using the well-known dispersion relation for parallel whistler waves (see e.g., Helliwell, 1965), which gives:

$$W_{\|\text{res}} = m_e c^2 \frac{\left(f_{\text{ce}} - f_w\right)^3}{2 f_w f_{\text{pe}}^2} \quad (1)$$

Here and further, f_w marks the frequency of narrow-banded whistler wave (see Figure 2), f_{ce} and f_{pe} denote electron cyclotron and electron plasma frequency, respectively, m is the electron mass, and c is the speed of light. For every instant of time during each interval of whistler bursts marked by "I–IV", we calculated the value of resonant energy $W_{\|\text{res}}$ using the local measurements of f_{ce}, f_{pe}, and f_w.

It is worth noting that the total energy of resonant electrons should be larger than $W_{\|\text{res}}$, so that $W_{\|\text{res}}$ represents the lower energy boundary of the resonant electrons interacting with the observed whistler waves.

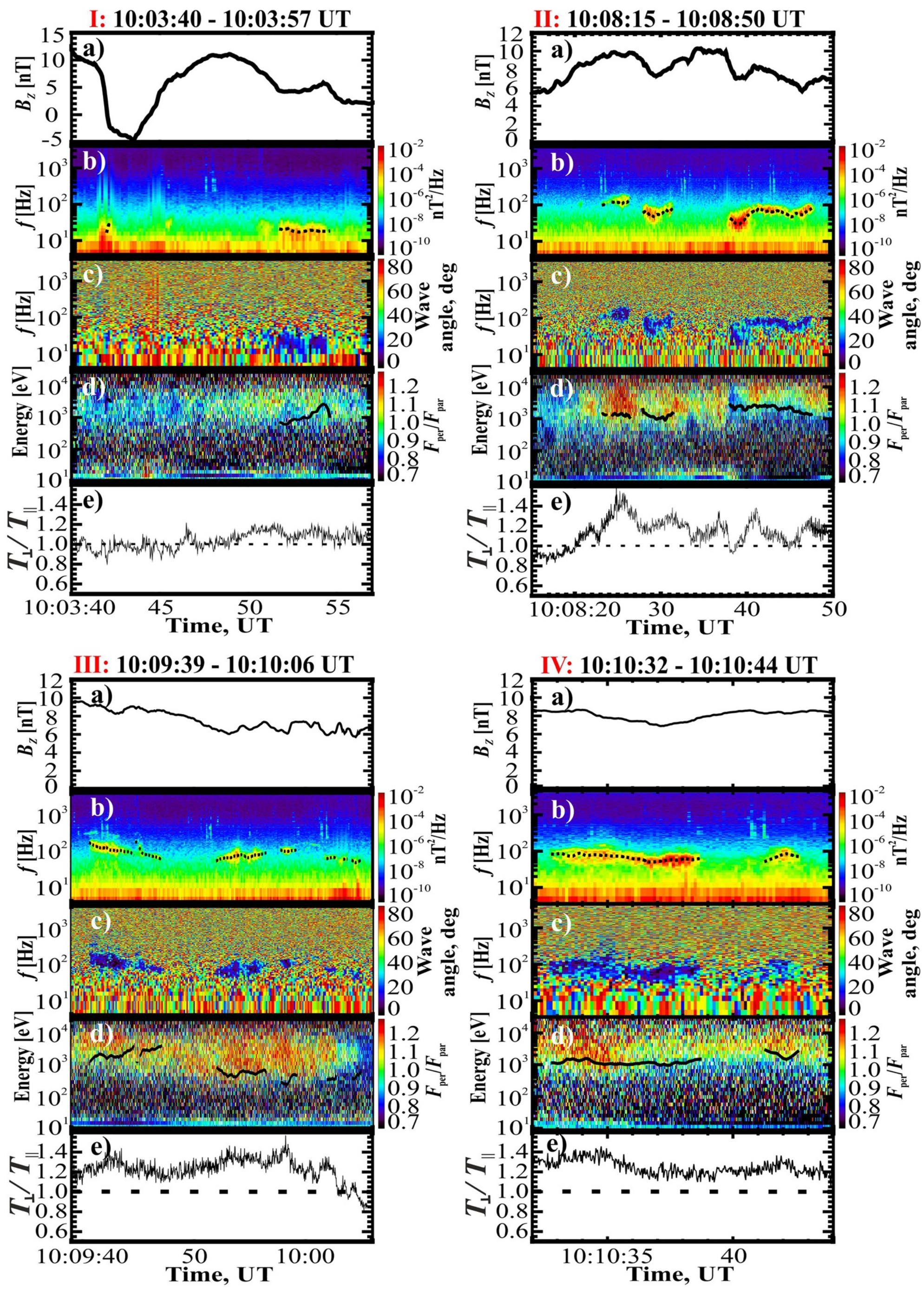

Figure 3. The dynamics of electron flux and temperature anisotropy during intervals "I–IV" of whistler bursts shown in Figure 1. In four corresponding blocks of panels there are (a) the B_Z field; (b) F–T spectrogram of the magnetic field fluctuations; (c) the wave normal angle; (d) the E–T spectrogram of the electron $F_{\mathrm{PER}}/F_{\mathrm{PAR}}$; and (e) $T_{\perp}$ / $T_{\|}$. The dotted black line in panel (b) of each block shows the whistler wave frequency f_w. The solid black line in panel (d) of each block displays the $W_{\|res}$.

Panels (d) of Figure 3 display the color-coded Energy–Time spectrograms of flux ratio $F_{\mathrm{PER}}/F_{\mathrm{PAR}}$ of electrons moving almost perpendicular (pitch angles close to 90°) and parallel to the ambient magnetic field. For F_{PAR}, we used either the electron flux corresponding to pitch angles close to 0° or 180° depending on which flux was larger. The quantity $W_{\|res}$ as a function of time is shown in each panel (d) by the solid black line.

The beginning of the majority of whistler bursts was associated with the increase in $T_\perp$ / $T_\|$ (shown in panels (e) of each blocks) and with the increase in F_{PER}/F_{PAR} > 1.1. By the end of these wave bursts, the electron perpendicular anisotropy decreased. The increase in F_{PER}/F_{PAR} was observed in a finite higher-energy range (>1 keV), and the time profile of $W_{\|res}$ marked the lower energy boundary of this energy range (see panels (d) in each block). Thus, during the intervals of whistler bursts, the observed perpendicular temperature anisotropy was caused by the perpendicular anisotropy of suprathermal electron population with energies ≥ $W_{\|res}$.

However, during the interval II in the beginning of the last whistler burst (at ∼10:08:38–10:08:39 UT), $T_\perp$ / $T_\|$ < 1.0 is observed. At these moments, the perpendicular anisotropy of electron flux is observed at very high energy range close to the high energy threshold of the FPI instrument (see panel (d) of the block II in Figure 3). This high-energy anisotropic electron population gives small contribution to the temperature anisotropy calculated from the entire energy range of the velocity distribution function. But this anisotropic population can interact and/or generate the observed whistler waves. Thus, in some cases of whistler wave observations, the condition $T_\perp$ / $T_\|$ > 1.0 is not fulfilled because of the instrumental limitation in observation of high energy resonant electrons. We return to this problem in the Discussion section and Figure 8.

2.3. The Calculation of the Growth Rate (γ) and Determination of the Characteristics of Resonant Electrons

In the previous subsection, we have calculated the parallel energies of resonant electrons ($W_{\|res}$) interacting with the observed quasi-parallel whistler waves and found that $W_{\|res}$ ranged from ∼600 eV to ∼ 5 keV during the observed whistler bursts (see Figure 3). The total energy of electrons which can efficiently interact with the whistler waves, W_{res}, should be larger than $W_{\|res}$. To determine W_{res} and pitch angles of the resonant electrons, α_{res}, we calculated the growth rate γ and studied its dynamics during short whistler bursts. For this analysis, we used the MMS burst mode observations of local 3D electron velocity distribution function measured with 30 ms time resolution.

The method for calculating the growth rate is described in detail in Grigorenko et al. (2020). Figure 4 shows the distribution of the normalized growth rate γ/ω_{ce} on the (*T*–*F*) plane, where the values γ/ω_{ce} themselves are shown by a color code. The growth rates were calculated based on the local distribution function measured during each burst of whistlers in the intervals I–IV. Data corresponding to the particular intervals are shown in separate blocks of panels. The growth rates were calculated for whistler waves propagating antiparallel ($\mathbf{k}\cdot\mathbf{B} < 0$) and parallel ($\mathbf{k}\cdot\mathbf{B} > 0$) to the external magnetic field **B**. The corresponding values are shown in panels (b) and (c), respectively. The frequencies of whistler waves are shown in these panels by the solid magenta lines. To calculate the growth rate, we used a 3D electron distribution function averaged over time interval of 120 ms. Such averaging is necessary in order to exclude sharp gradients of the distribution function in the phase space associated with the random appearance of zeros in some energy and pitch-angle channels (recall that the growth rate is essentially determined by the gradients of the distribution function in the phase space). For completeness, panel (a) of each block shows a spectrogram of magnetic field fluctuations. The variation of the frequency f_w in time is shown in this panel by the black dashed line. The distribution of the quantity γ/ω_{ce} on the (*T*–*F*) plane is somewhat different for waves propagating parallel and antiparallel with respect to **B**. This means that there is some asymmetry in the electron distribution function with respect to the pitch angle of 90°. However, the growth rates for such waves are close in absolute value.

To find out the characteristics of resonant electrons which interact efficiently with whistler waves and contribute to their generation, we have determined the pitch angles α_{res} and total energies $W_{res} = W_{\|res}/\cos^2\alpha_{res}$ for electrons that make maximum positive contribution to the maximal growth rate γ at each instant of time during every wave burst. The time profiles of α_{res} and W_{res} calculated for waves propagating parallel and antiparallel to **B** are shown respectively by the red and blue lines in panels (d) and (e) of each block. At the time points when the observed wave frequency f_w was in the frequency range of positive γ, the values of α_{res} were in the range from 30° to 80° for resonant electrons interacting with antiparallel propagating waves, and in the range from 100° to 150° for electrons interacting with parallel propagating waves (we remind the reader that in this study we only take into account the resonance wave-electron interaction at the first cyclotron resonance.) This is consistent with the idea that the perpendicular anisotropy of electron distribution is the main cause of instability in the cases under discussion.

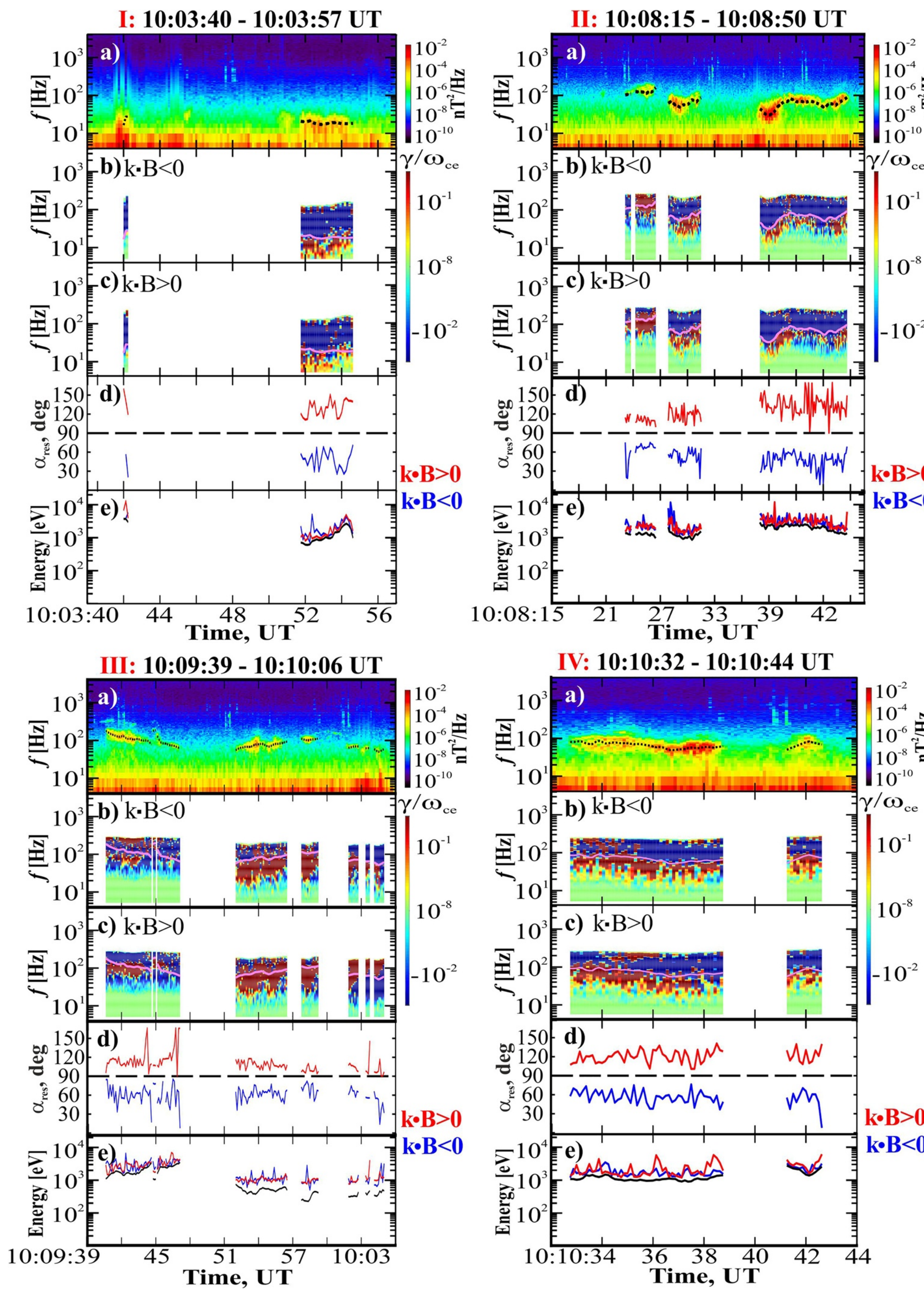

Figure 4. The dynamics of the normalized growth rate value (γ/ω_{ce}) and the characteristics of resonant electrons during intervals "I–IV" of whistler bursts shown in Figure 1. In four corresponding blocks of panels there are (a) *F–T* spectrogram of the magnetic field fluctuations; (b) the quantity γ/ω_{ce} calculated for the whistler waves propagating anti-parallel; and (c) parallel to **B** ; (d) the time profiles of α_{res} of electrons contributing to the maximum of γ for the waves with $\mathbf{k}\cdot\mathbf{B} > 0$ (shown by red) and for the waves with $\mathbf{k}\cdot\mathbf{B} < 0$ (shown by blue); and (e) the time profiles of W_{res} of electrons contributing to the maximum of γ making maximum contribution to γ for the waves with $\mathbf{k}\cdot\mathbf{B} > 0$ (shown in red) and for the waves with $\mathbf{k}\cdot\mathbf{B} < 0$ (shown in blue). Black dotted lines in panels (a) and solid magenta lines in panels (b) and (c) display the frequency f_w of the observed whistler waves, respectively. Solid black lines in panels (e) display the time profiles of $W_{||res}$.

The total energy of resonant electrons W_{res} is also highly variable within each burst (see panel (e) in each block of Figure 4). In panel (e) of each block, we also display by the black line the time profile of the parallel energy of resonant electrons $W_{||res}$ for reference. At those instants of time, when f_w was in the frequency band of positive γ, the values of W_{res} were in the range from 1 to 10 keV corresponding to energy span of perpendicular anisotropy of electron flux as it is seen from panes (d) of Figure 3. Thus, thermal and suprathermal electrons should interact efficiently with the observed whistler waves. This, in turn, causes the variations of anisotropy of electron velocity distribution function observed in this energy range.

For the majority of wave bursts, there is a rather good agreement between the observed f_w and the frequency at which the maximum value of γ/ω_{ce} is found from calculations (f_γ). This indicates that the anisotropy of local velocity distribution function can be responsible for the generation of the observed whistler waves, that is, the spacecraft is located close to the source. Indeed, during this time, MMS was located close to the equatorial plane ($|B_X| \leq 5$ nT), where the source of whistler waves is most likely located (e.g., Khotyaintsev et al., 2011; Le Contel et al., 2009). At those moments when the observed wave frequency differs significantly from f_γ, the wave should have arrived to the observation point from a remote source, and the quantities α_{res} and W_{res} could be determined incorrectly. Thus, for statistical analysis of the characteristics of resonant electrons, we determine α_{res} and W_{res} only at those moments when the criterion:

$$\left|f_w - f_\gamma\right| / f_w < 0.1 \quad (2)$$

is fulfilled.

3. Statistical Studies of the Characteristics of Resonant Electrons

To determine statistically the characteristics of resonant electrons interacting with the quasi-parallel whistler waves during prolonged dipolarizations, we have analyzed MMS observations in the PS at -22 $R_E < X \leq -8$ R_E and $|Y_{GSM}| \leq 10$ R_E from May to October 2017. During this period, we have found 150 prolonged dipolarizations, but observations in the burst mode were available only in 48 events from our data base. In these events, we have identified 163 bursts of quasi-parallel narrowband whistler waves similar to that presented in Figures 1 and 2. A full list of dipolarization events with the burst mode observations along with the whistler burst intervals is given in Supporting Information.

In order to identify these waves, we have analyzed the frequency spectra of magnetic field fluctuations δB measured by SCM at each instant of time for those dipolarization events from our data base for which the observations in the burst mode were available. For each instant of time, we look for a local maximum or a bulge in the frequency spectrum between the lower hybrid (f_{LH}) and electron cyclotron (f_{ce}) frequency where the whistler waves related to dipolarizations are observed most often (e.g., Liang et al., 2012). We find local spectral maximum using the method of gradient descent (e.g., Akilov & Kantorovich, 1982) just as it was done by Grigorenko et al. (2020). To be sure that the bulge in each spectrum represents the quasi-parallel whistler wave, we check the condition for the wave normal angle to be less than 40° and the degree of polarization >0.7. In total, we have obtained 2,688 wave measurements taken at various moments of time within all bursts from our data base, which we will further term wave moments. For each such moment, we analyzed electron velocity distribution function and calculated the growth rate γ.

In order to show statistically the distribution of the detected quasi-parallel whistler bursts over the prolonged dipolarization events from our data base, we apply a superposed epoch analysis to 48 dipolarization events in which the burst mode observations were available. The epoch analysis was applied to the B_Z field and the X component of ion bulk velocity (V_X). For each event, the B_Z field was normalized to the corresponding maximum value (B_{Z_max}) observed within 30 s interval after the onset of a given dipolarization: $B_Z{}^* = B_Z(t)/B_{Z\_max}$. The V_X in each dipolarization event was normalized to the maximum value (V_{X_max}) observed during the entire interval of a given dipolarization event: $V_X{}^* = V_X(t)/V_{X\_max}$. As the epoch time ($t_0 = 0$), we use the dipolarization onset similarly to the previous study by, for example, Grigorenko et al. (2016).

Figure 5 presents the results of the epoch analysis. The epoch profiles of $V_X{}^*$ and $B_Z{}^*$ are shown in Figures 5c and 5d, respectively. The onset of dipolarizations from our data base was associated with arrival of high speed bulk flows. In Figure 5a, we display the distribution of probability of the burst mode operation

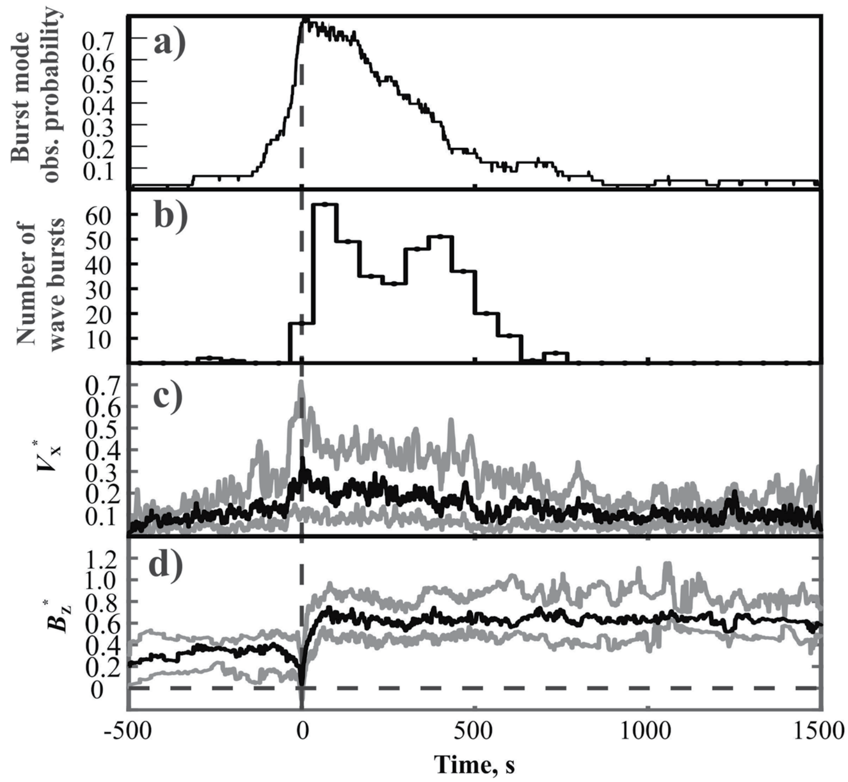

Figure 5. The epoch analysis of the prolonged dipolarizations in which quasi-parallel whistler waves were observed. From top to bottom: (a) the distribution of probability of the burst mode operation; (b) the number of detected whistler bursts; (c) the epoch profiles of V_X*; and (d) B_Z*. The vertical dashed line marks the zero epoch time corresponding to the dipolarization onset.

over the dipolarization events from our data base. In Figure 5b, we show the number of detected bursts of quasi-parallel whistler waves. Unfortunately, the majority of the burst mode observations took place solely during ~300 s after the dipolarization onset. At the later stage of dipolarization during the interval of B_Z relaxation, the burst mode observations are rare or completely absent. Thus, we have information on whistler wave observations only within ~13 min following the dipolarization onset.

The majority of whistler waves from our data base have durations ~ 0.25–2.5 s. However, there are a few bursts with longer durations, up to ~9.5 s (see Figure 6a). The majority of waves have frequencies $f_w \le 0.2 f_{ce}$ (see blue histogram in Figure 6b). The corresponding normalized frequencies are lower than that of quasi-parallel whistler waves observed in single DFs by Grigorenko et al., 2020. As a result, the parallel energies of resonant electrons $W_{||res}$ are statistically higher than the energies of resonant electrons interacting with whistler waves in the isolated DFs. Indeed, as it is seen from Figure 6c, in ~ 48% of events the $W_{||res} \ge 10$ keV. This means that in many cases the total energy of resonant electrons may approach or be even higher than the high-energy threshold of the FPI instrument.

In Figure 6d, we present three distributions of probability to observe the quasi-parallel whistler waves versus given local value of electron temperature anisotropy $T_\perp / T_{||}$. The blue histogram was obtained by using all wave moments from our data base. While ~70% of whistler waves observed in isolated DFs were associated with the perpendicular electron anisotropy $T_\perp / T_{||}$ (Grigorenko et al., 2020), during the prolonged dipolarizations a lot of whistler waves were observed when $T_\perp / T_{||} \le 1.0$. This contradicts the expectation that perpendicular temperature anisotropy can be the prime cause of whistler waves. Since in our data base there are wave moments at which whistler waves propagate to the spacecraft from a remote source (condition (2) is not fulfilled), we plot in Figure 6d the distribution, shown in magenta, which was constructed using only those wave moments at which condition (2) was fulfilled. At such moments, the anisotropy of local electron velocity distribution function can be responsible for the wave generation. Nevertheless,

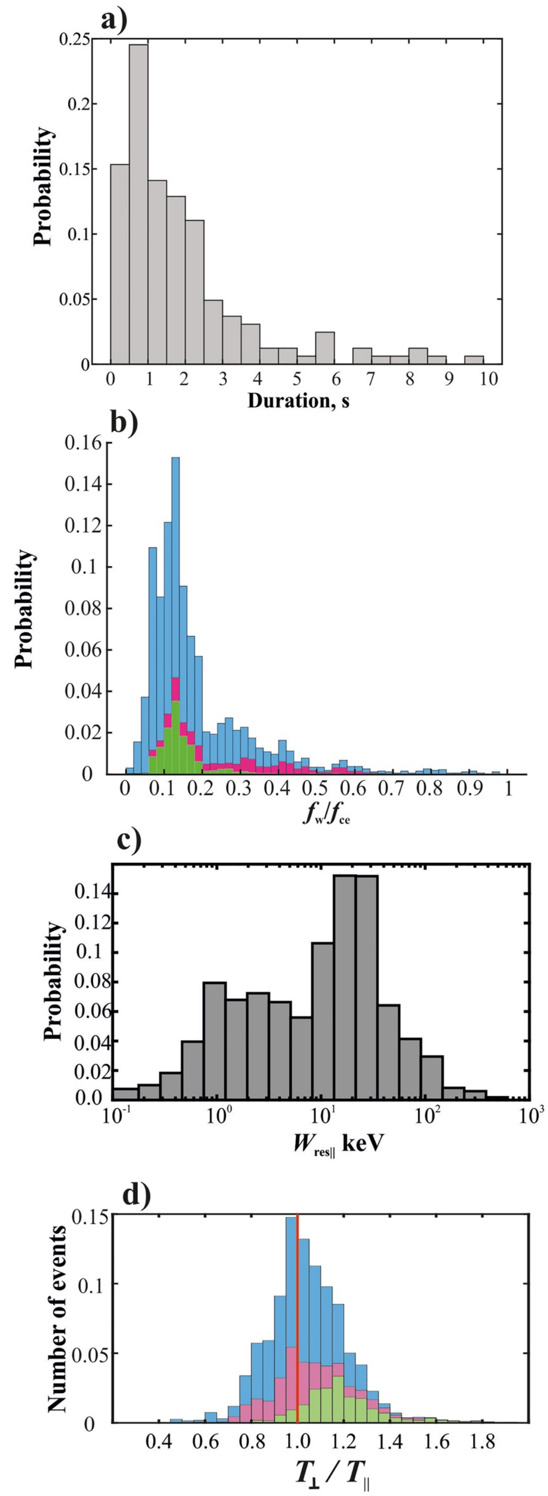

Figure 6. From top to bottom: (a) the distributions of probability to observe the whistler bursts with a given duration; (b) with a given values of wave frequency (f_w) normalized to the local f_{ce}. The blue histogram displays the distribution of probability obtained by using all wave bursts from our data base. The magenta histogram shows the distribution which was constructed by using only those wave moments at which condition (2) was fulfilled. The green histogram presents the distribution obtained by using those moments at which condition (2) was fulfilled and at which the observed waves were potentially capable to scatter electrons into the loss cone. Panel (c) shows the distribution of $W_{||res}$ calculated for all wave moments present in our data base. Panel (d) shows the distributions of wave moment number versus the observed values of $T_\perp$ / $T_{||}$. In this panel the histogram shown in blue was obtained using all wave moments from our data base. The histogram shown in magenta was constructed using only those wave moments at which condition (2) was fulfilled. The histogram shown in green was obtained using those wave moments at which condition (2) was fulfilled and $W_{||res} \leq 5$ keV.

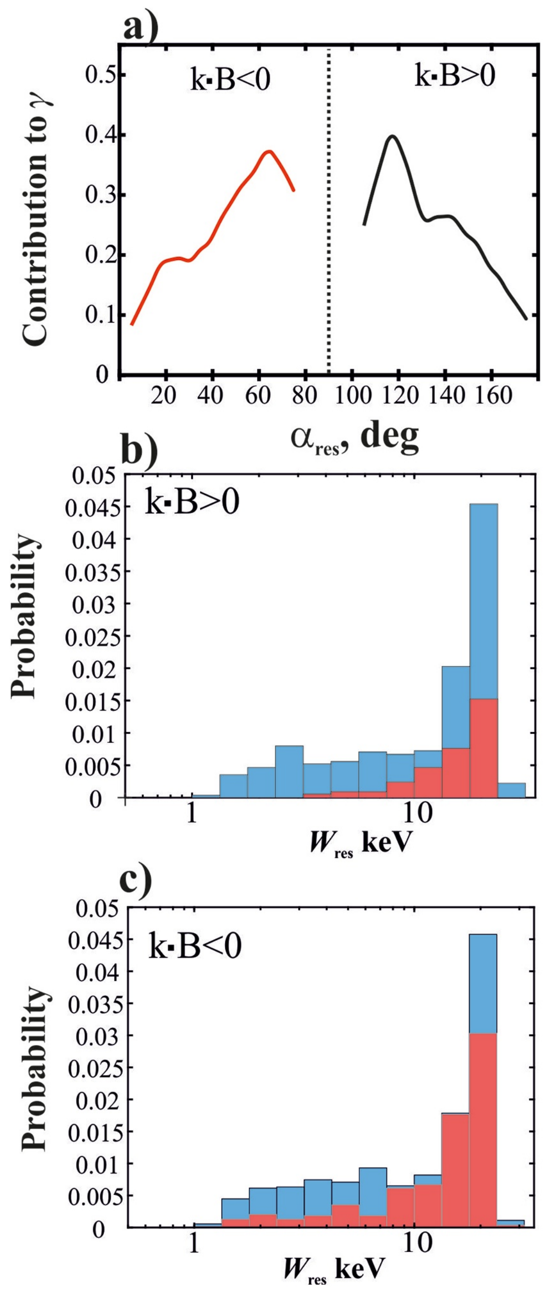

Figure 7. From top to bottom: (a) the median profiles of the normalized values of positive contribution of resonant electrons to the maximal γ as a function of electron pitch angles (α_{res}) for the waves propagating parallel (black profile) and anti-parallel to **B** (red profile); (b) the statistical distributions of W_{res} of electrons which make the maximal contribution to γ for the waves with $\mathbf{k}\cdot\mathbf{B} > 0$; and (c) $\mathbf{k}\cdot\mathbf{B} < 0$. The blue histograms present the distribution of W_{res} calculated for the moments at which condition (2) was fulfilled. The red histograms display the distributions of W_{res} of the resonant electrons which could be potentially scattered into the loss cone by the observed whistler waves.

in this distribution there are still a number of wave moments at which $T_\perp / T_\parallel \leq 1.0$. In Section 2.2, it has been shown that if $W_{\parallel res}$ is rather large, the perpendicular anisotropy of electron flux can be observed at very high energy range close to or even above the high-energy threshold of the FPI instrument. In such cases, the value of $T_\perp / T_\parallel$ deduced from the energy range covered by the FPI does not contain an information on the real anisotropy of resonant electron population. To check this, we constructed the distribution of probability to observe whistler waves using only those wave moments at which not only condition (2) was fulfilled but also $W_{\parallel res} \leq 5$ keV. The last ensures that the total energy of resonant electrons is within the energy range of the FPI instrument (see the green distribution in Figure 6d). This distribution demonstrates that almost at all such moments $T_\perp / T_\parallel > 1.0$. Thus, the contradiction to the expectation that perpendicular temperature anisotropy can be the prime cause of whistler waves is delusive because it is caused by the limitation of the FPI instrument which is unable to observe the high-energy part of electron velocity distribution function. It is this non-observed high-energy part of the velocity distribution function which is expected to resonantly interact with the low-frequency whistler waves. We return to this problem in the Discussion section.

To define statistically the characteristic energies (W_{res}) and pitch angles (α_{res}) of resonant electrons interacting with the quasi-parallel whistler waves during the prolonged dipolarizations, we calculate these values at those time moments during each burst when the observed wave frequency (f_w) is close to the frequency corresponding to the maximum value of the growth rate (f_γ), that is, at those moments when condition (2) is fulfilled. At such moments, MMS can be located close to the wave source. In Figure 6b, we present the statistical distribution of wave frequencies observed at such moments (the magenta-shaded histogram). Condition (2) is fulfilled for ~26% of the total number of wave moments from our data base both for the wave propagating parallel and antiparallel to the ambient magnetic field. The majority of these waves have frequencies $f_w \sim (0.1\text{–}0.2) f_{ce}$. Then, we determine α_{res} and the corresponding values of the total energies of resonant electrons $W_{res} = W_{\parallel res}/\cos^2\alpha_{res}$, which make the major positive contribution to γ according to Equation 1 in Grigorenko et al. (2020).

Figure 7a presents the median profiles of the normalized values of positive contribution of resonant electrons to the maximal γ in dependence on electron pitch angles (α_{res}). The black profile corresponds to electrons interacting with the waves propagating parallel to **B** ($\mathbf{k}\cdot\mathbf{B} > 0$), while the red profile corresponds to electrons interacting with the waves propagating antiparallel to **B** ($\mathbf{k}\cdot\mathbf{B} < 0$). For the waves with $\mathbf{k}\cdot\mathbf{B} > 0$, the maximum contribution to γ is made by electrons with $\alpha_{res} \sim 100°\text{–}130°$, and for the waves with $\mathbf{k}\cdot\mathbf{B} < 0$ electrons with $\alpha_{res} \sim 50°\text{–}80°$ make the maximal contribution to γ. The parity of local growth rates for waves propagating in different directions by no means implies that they have comparable amplitudes, as the latter is determined by integral amplification coefficient which should be larger for waves that crossed the equatorial region where the magnitude of the growth rate is maximal.

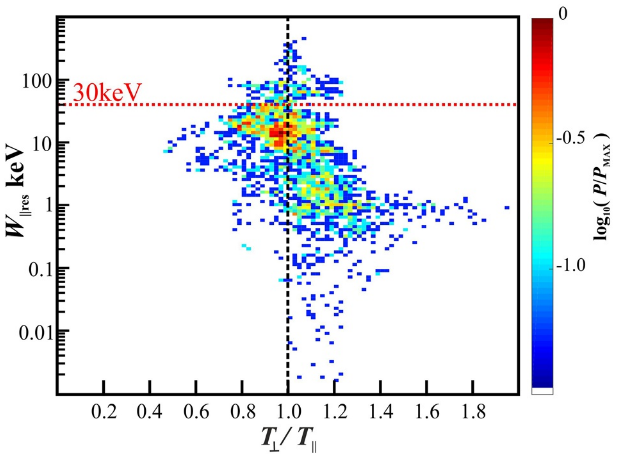

Figure 8. A color-coded distribution of probability (P/P_{MAX}) to observe at each moment of time within each whistler burst the values of $W_{\|res}$ and $T_\perp$ / $T_\|$ within a given bin. The horizontal red dotted line displays the high-energy threshold of the FPI instrument.

Figures 7b and 7c show the statistical distributions of W_{res} of electrons which make the maximal contribution to γ for the waves with $\mathbf{k}\cdot\mathbf{B} > 0$ and $\mathbf{k}\cdot\mathbf{B} < 0$, respectively. In the majority of cases, W_{res} is large and exceeds 10 keV both for the waves propagating parallel and antiparallel to **B**.

Thus, suprathermal electrons (the kinetic energy of such electrons is several times larger than their thermal energy) with pitch angles rather close to ∼65° and ∼115° and moving in the opposite direction to the waves efficiently interact with the quasi-parallel whistler waves. In terms of pitch angles, this result agrees with the corresponding characteristics of resonant electrons interacting with quasi-parallel whistler waves at isolated DFs registered farther from the Earth (Grigorenko et al., 2020). However, the values of W_{res} are higher during the prolonged dipolarizations than in isolated DFs. We discuss this point in the next section. It is worth mentioning that when we speak about electrons making the main contribution to the growth rate, we always mean the frequency of maximum γ, that is, the frequency corresponding to the most unstable wave.

4. Discussion

Using the burst mode MMS observations, we have determined the energy and pitch-angle characteristics of resonant electrons interacting with the quasi-parallel whistler waves during the prolonged dipolarizations in the near-Earth magnetotail. The dipolarization events from our data base represent a complicated perturbation of the B_Z field comprising multiple B_Z pulses and a prolonged interval of the B_Z relaxation lasting from several minutes to approximately half an hour. All dipolarizations were associated with the high velocity ion bulk flows and they were observed at $-22\ R_E < X \leq -8\ R_E$. A phase velocity of quasi-parallel whistler waves (V_w) from our data base ranged from ∼5,000 km/s to a few tens of thousands km/s. Thus, for such bursts Doppler shift was negligible. Indeed, for events observed near the equatorial plane (the majority of bursts in our data base), V_w was directed almost perpendicular to the velocity of ion bulk flows (V_X), so that the ion bulk velocity along the magnetic field line (∼along Z) was hundred(s) time smaller than V_w. For those wave bursts which were observed well outside the equatorial plane, V_w was of the order of a few hundreds of thousands km/s due to the large local f_{ce}. For such events, Doppler shift also was approximately a few percent of the wave frequency or less.

Unfortunately, in all events from our data base, the burst mode was available only within ∼13 min following the dipolarization onset (see Figure 5). For the events from our data base, this interval covers the major part of a high velocity bulk flow(s) along with the multiple B_Z pulses which most likely represent Dipolarizing Flux Bundles (DFBs) (e.g., Liu et al., 2013, 2014). Thus, the results presented in our paper concern the electron population which characteristics experience the strongest modification due to the interaction with the whistler waves in the beginning of dipolarization. But the present results do not give any information on the observation of whistler waves and the characteristics of resonant electrons during the interval of the B_Z relaxation. Before discussing our results, we summarize the characteristics of the whistler waves observed during the prolonged dipolarizations.

1. The majority of the narrowband quasi-parallel whistler waves have frequencies $f_w \leq 0.2 f_{ce}$. The duration of whistler bursts ranges from ∼0.25 to ∼2.5 s.
2. A significant fraction of whistler bursts were detected along with $T_\perp$ / $T_\| \leq 1.0$.
3. Electrons with pitch angles $\alpha_{res} \sim$ 100°–130° and $\alpha_{res} \sim$ 50°–80° made maximum contribution to the growth rate of whistler waves propagating quasi-parallel ($\mathbf{k}\cdot\mathbf{B} > 0$) and antiparallel ($\mathbf{k}\cdot\mathbf{B} < 0$) to the ambient magnetic field, respectively (see Figure 7a).
4. For the majority of events from our data base, the total energy of electrons making positive contribution to the growth rate was ≥10 keV (Figures 7b and 7c).

Statistically, the relative frequencies of whistler bursts (f_w/f_{ce}) observed during dipolarizations in the near-Earth tail are lower than the frequencies of whistler waves detected in isolated DFs farther from the Earth (Grigorenko et al., 2020). This results in the increase in energy of resonant electrons interacting with the whistler waves in the near-Earth tail. The large values of W_{res} imply that only small high-energy fraction of electron velocity distribution measured by the FPI interacts with the whistler waves. As it was shown in Subsection 2.2, during the intervals when the energy of resonant electrons approaches the high-energy threshold of the FPI instrument, the perpendicular anisotropy of electron flux is observed in a finite high-energy part of the spectrum. Such small high-energy fraction of electron velocity distribution does not contribute much to the value of temperature anisotropy calculated for the entire range of energy spectrum. As a result, at such moments $T_\perp / T_\| \le 1.0$ may be observed (see Figures 3d and 3e for the burst II), although the high-energy part of electron distribution efficiently interacting with the whistler wave has the perpendicular anisotropy.

To demonstrate this effect statistically, we plot in Figure 8 a color-coded distribution of probability (P/P_{MAX}) to observe at each moment of time within each whistler burst the values of $W_{\|res}$ and $T_\perp / T_\|$ within a given bin. The probability (P) was normalized to the maximum value of probability observed in all events from our data base (P_{MAX}).

It is seen from the figure that in the majority of those moments when $T_\perp / T_\| < 1.0$, the values of $W_{\|res}$ are rather high and approach to the high-energy threshold of the FPI instrument. At such moments, the total energies of resonant electrons (W_{res}) are expected to be larger than $W_{\|res}$ and may exceed the high-energy threshold of FPI instrument (30 keV). Indeed, the core of distribution which is characterized by the large values of P/P_{MAX} is observed inside the interval of $W_{\|res} \sim$ 10–30 keV and the corresponding $T_\perp / T_\| \sim$ 0.8–1.05. Because of the large values of $W_{\|res}$ and, thus, W_{res}, the corresponding values of $T_\perp / T_\|$ calculated for the energy range of the instrument may not represent correctly the real anisotropy of that part of the electron velocity distribution function which could be responsible for the whistler wave generation. Thus, the conclusion drawn from Figure 8 allows us to suggest that the whistlers observed during periods when $T_\perp / T_\| < 1.0$ due to the high-energy range limitation of the instrument may still have originated locally and by the same mechanism as whistlers observed during periods with clear perpendicular electron anisotropy. Indeed, in the majority of moments when $W_{\|res}$ is well inside the energy range measured by FPI (<10 keV), $T_\perp / T_\| > 1.0$, and we may suggest that the observed whistler waves were excited due to cyclotron instability.

In the previous section, we statistically demonstrated that the maximum positive contribution to the growth rate (γ) of whistler waves is made mostly by electrons with total energies $W_{res} \ge 10$ keV and pitch angles $\alpha_{res} \sim 100°$–$130°$ and $\alpha_{res} \sim 50°$–$80°$ for the waves propagating quasi-parallel and antiparallel to **B**, respectively. Electrons which make the positive contribution to γ transfer their energy to the wave and, as a result, their pitch angle decreases. Indeed, in the case of parallel propagation of whistler-mode waves, the variations of resonant particle kinetic energy W_{res} and magnetic momentum $\mu = mV_\perp^2 / 2\omega_{ce}$ are related by (see e.g., Karpman et al., 1974):

$$\Delta\mu = \frac{\Delta W_{res}}{\omega},$$

where ω is the wave angular frequency: $\omega = 2\pi \cdot f_w$. With the help of this relation, the variation of the quantity

$$\sin^2\alpha_{eq} = \frac{\mu\omega_{ceq}}{W_{res}}$$

(ω_{ceq} is electron equatorial gyrofrequency), which is the sine squared of particle equatorial pitch angle (α_{eq}), can be expressed through ΔW_{res}, and is given by:

$$\Delta\left(\sin^2\alpha_{eq}\right) = \left(\frac{\omega_{ceq}}{\omega} - \sin^2\alpha_{eq}\right)\frac{\Delta W_{res}}{W_{res}}.$$

Since for whistler waves $\omega < \omega_{ceq}$, the variation of particle equatorial pitch angle has always the sign of energy variation. That is, why the particles, which make a positive contribution to the growth rate γ and, thus, loose their energy, have always their equatorial pitch angle decreased and may be precipitated into the loss cone.

In this respect, it is important to determine the energy of resonant electrons which can be scattered into the loss cone in the course of their interaction with the whistler waves. Since at the distances where events from our data base are observed the loss cone angle is very small (~a few degrees), the angular resolution of the FPI instrument is not sufficient to observe the loss cone electron population. We can only determine the energies of resonant electrons which initially have the minimal pitch angles but still make the positive contribution to γ. From Figure 7a, it is seen that such electrons have pitch angles in the ranges 0°–25° and 155°–180° for the waves propagating antiparallel and quasi-parallel to **B**, respectively. Such electrons can potentially be scattered into the loss cone. A quantitative characteristics of electron precipitation caused by resonant interaction with whistler bursts under discussion is out of the scope of the present study.

In Figures 7b and 7c, we display the red-shaded statistical distributions of W_{res} of electrons, which can be potentially scattered into the loss cone in the course of interaction with the waves propagating quasi-parallel and antiparallel to **B**, respectively. For both directions of the wave propagation in the majority of cases such electrons have $W_{\mathrm{res}} \sim$ 10–20 keV. The scattering of these electrons into the loss cone can contribute to electron precipitation in the auroral region during ~13 min following the dipolarization onset. It is worth noting that for determination of W_{res} we used only those moments of wave observations when condition (2) was fulfilled, that is, when the frequency corresponding to the maximum of γ calculated from the local electron distribution function was almost equal to the observed wave frequency. Unfortunately, we do not have any information on the properties of whistler waves and resonant electrons which could be observed at the later stage of dipolarization because of the absence of burst mode observations.

To reveal the frequencies of whistler waves which can scatter electrons into the loss cone, we select the moments of wave observations at which electrons with small initial pitch angles make the positive contribution to γ and condition (2) is fulfilled. In Figure 6b, we present the statistical distribution of wave frequencies observed at such moments (the green-shaded histogram). It is seen that the majority of whistler waves capable to scatter electrons into the loss cone have low frequencies ~(0.05–0.2)f_{ce}.

In the previous studies, it was shown that, in unstable plasma, the energy from lower-energy electron population can be transferred to higher-energy population via wave-particle interactions (e.g., Grigorenko et al., 2020; Shklyar, 2011, 2017). To check this possibility for the events from our data base, we determine α_{res} and the corresponding values of W_{res} of electrons which make the maximum negative contribution to γ. Such electrons obtain energy from the wave. This leads to an increase in electron pitch angles and the perpendicular anisotropy of the corresponding part of velocity distribution function.

In order to study a wave mediated energy exchange between different electron populations, it is needed to cover both the entire pitch angle and energy ranges observed by FPI instrument. Therefore, we have limited our analysis in the range of parallel energies $W_{\|\mathrm{res}}$ from ~0.6 to ~2.5 keV (see for example, the purple, green, and light-blue curves of $W_{\mathrm{res}}(\alpha)$ in Figure 9a). Figures 9b and 9c display the statistical distribution of α_{res} for electrons making maximal positive and negative contributions to γ, respectively. Both distributions are almost similar and maximize at $\alpha_{\mathrm{res}} \sim$ 60°–65° and ~115°–120° for the waves propagating antiparallel and quasi-parallel to the **B**, respectively. Thus, the quasi-perpendicular electrons participate in the most efficient energy exchange with the observed quasi-parallel whistler waves.

Figures 9d and 9e show the statistical distribution of W_{res} for electrons making maximal positive and negative contributions to γ, respectively. It is seen that these distributions are quite different. While the maximal positive contribution is made mostly by electrons with $W_{\mathrm{res}} \sim$ 2–6 keV, the maximal negative contribution is mostly made by electrons with $W_{\mathrm{res}} \sim$ 3–13 keV, that is, the higher-energy population obtains the energy from the waves. This effect is similar, but not identical, to energy transfer in the case of oblique propagation (Shklyar, 2017). Let us discuss this point in more detail.

In the case of oblique propagation, the first cyclotron and Landau resonances play the most important role as they correspond to lower magnitude of parallel velocities $V_{\|} = V_{r1} \equiv \left(\omega - \omega_{\mathrm{ce}}\right) / k_{\|}$ and $V_{\|} = V_{r0} \equiv \omega / k_{\|}$. At the same time, for a wide class of energetic electron distribution, the growth rate related to the first cyclotron resonance is positive, while the growth rate related to Landau resonance is negative. Since the sum of

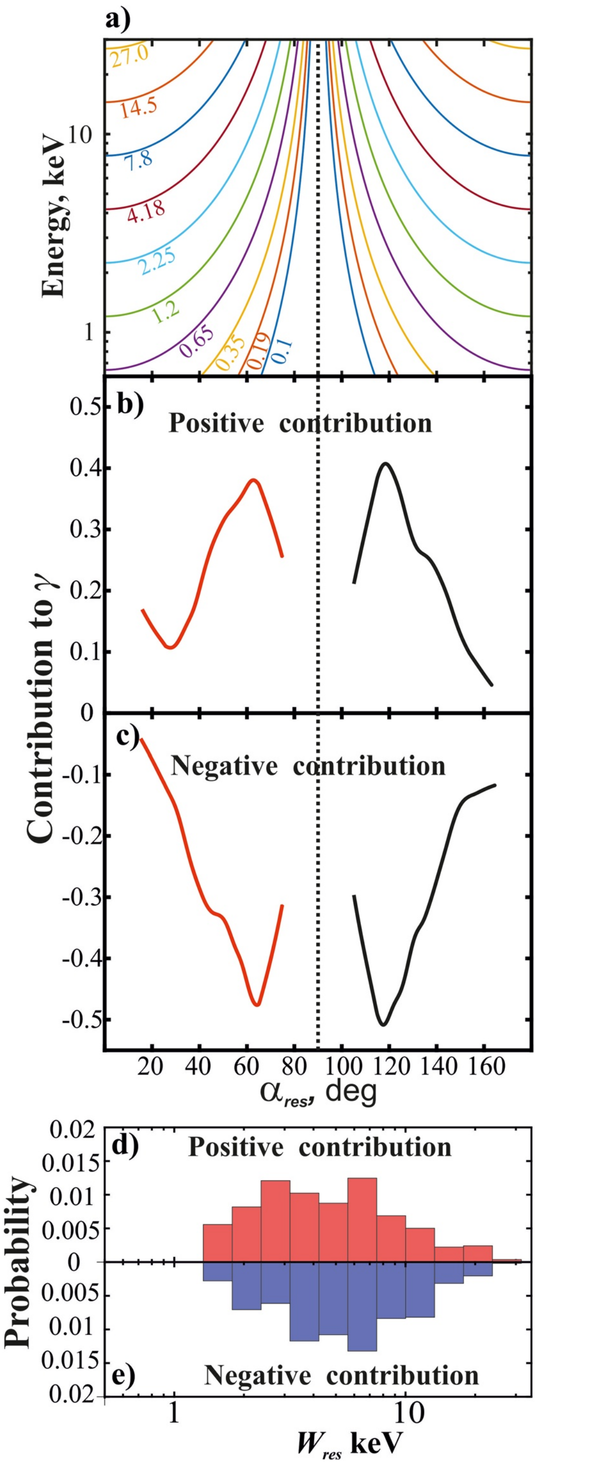

Figure 9. From top to bottom: (a) the colored curves of $W_{res}(\alpha)$ calculated for a given $W_{||res}$, which value in keV is displayed near the corresponding curve; (b) the median profiles of the normalized values of positive; and (c) negative contributions of resonant electrons to the maximal γ in dependence on electron pitch angles (α_{res}). The profiles obtained for the waves propagating parallel and anti-parallel to **B** are displayed by black and red lines, respectively. Panels (d) and (e) show the distributions of W_{res} of electrons making maximal positive and negative contributions to γ, respectively.

wave energy and kinetic energy of resonant electrons is conserved, these imply that, on the average, the first cyclotron resonance particles lose their energy, while Landau resonance particles gain the energy. Thus, in the case of oblique propagation, a wave mediated energy exchange takes place between electrons with various parallel velocities. In the case of parallel propagation, all resonant particles have their parallel velocities close to $\left(\omega - \omega_{ce}\right) / k$. However, the sign of their contribution to the growth rate, after averaging with respect to gyrophase and parallel velocities inside the resonant region, depends on their perpendicular velocity or, equivalently, on pitch angle at a fixed parallel velocity equal to resonance one. And again, by energy conservation, particles making positive contribution to the growth rate lose their energy and vice versa. Thus, wave-particle interaction in the case of parallel propagation under discussion leads to energy exchange between electrons with different pitch angles (i.e., with different total energies).

We would like to stress that there is no contradiction in the statistical distributions of total resonant energies (W_{res}) of electrons making a positive contribution to γ presented in Figures 7b, 7c and 9d. While the distributions presented in Figures 7b and 7c were obtained by using the entire range of parallel energies $W_{||res}$ observed by FPI (the integration was made along the curves covering all range of $W_{||res}$ observed by FPI, see Figure 9a), the distribution displayed in Figure 9d was obtained only for the limited range of $W_{||res}$ (~0.6–2.5 keV) in order to cover the whole range of electron pitch angles and to determine the W_{res} of electrons making positive and negative contribution for a given value of $W_{||res}$. Since the pitch-angle distribution of resonant electrons maximizes at $\alpha_{res} \sim 60$–65° and ~115–120° (see Figures 7b and 7c), the limitation in the range of $W_{||res}$ results in the decrease in a number of FPI observations in high energy range (≥10 keV) corresponding to α_{res}. Thus, because of the upper-energy threshold of the FPI instrument ~30 keV, we cannot study the effect of energy exchange between electrons with different total energies in the higher energy range (≥10 keV). In the cases when higher energy electrons make a positive contribution to the growth rate and, thus, loose their energy, we may expect that the electron population, which makes a negative contribution to γ and obtain energy from the wave could have even higher energies not registered by the FPI.

As it was discussed above, the particles which make a positive contribution to the growth rate γ and, thus, loose their energy, have always their pitch angle decreased and vice versa. Thus, in the course of wave-electron interactions, the perpendicular anisotropy of the lower-energy part of velocity distribution should decrease while the higher-energy part of the distribution should increase its perpendicular anisotropy. Such processes of energy exchange between different parts of electron spectrum can lead to the transformation of the high-energy part of the spectrum from Maxwellian to the power law shape. Our finding is consistent with the previous observations of the power law shape of high-energy part of electron spectra in association with whistler waves during dipolarizations (e.g., Malykhin, Grigorenko, Kronberg, Koleva, et al., 2018; Zhao et al., 2019). The increase in perpendicular anisotropy of electron velocity distribution function in the high energy range, which is close or even exceeds the high-energy threshold of FPI instrument, and simultaneous decrease in the perpendicular anisotropy in the lower-energy range can lead to the values of $T_\perp / T_\parallel < 1.0$ during some whistler bursts.

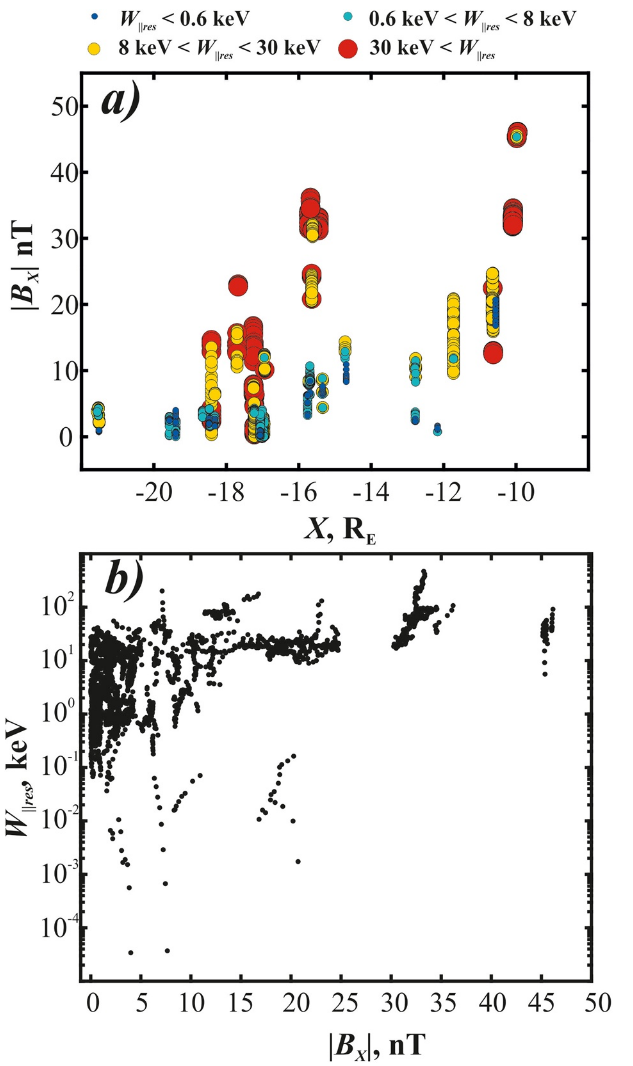

Figure 10. (a) The distribution of the observed whistler waves in the ($|B_X|$, X) parametric space. Each wave moment is displayed by the colored circle according to the corresponding value of electron $W_{\|\mathrm{res}}$ (shown at the top of the Figure). (b) A scatterplot of $W_{\|\mathrm{res}}$ versus $|B_X|$.

During the prolonged dipolarizations considered in the present study the parallel and, so, the total energies of resonant electrons were statistically higher ($W_{\mathrm{res}} \geq 10$ keV) than the W_{res} observed in the isolated DFs by Grigorenko et al., 2020. The majority of the isolated DFs were observed at $X < -20$ R_E and in the central part of the PS ($|B_X| \leq 10$ nT), while the prolonged dipolarizations analyzed in this paper were observed in a larger range of X and $|B_X|$. Since the value of the parallel resonant energy $W_{\|\mathrm{res}}$ depends on the local f_{ce} (see Equation 1 in Section 2.2) one may expect that the statistically higher resonant energies reported in the present study are due to the spacecraft location in the region with larger $|\mathbf{B}|$, that is, in the outer PS and/or closer to the Earth. To check this, we plot in Figure 10a the distribution of the wave bursts from our data base in the ($|B_X|$, X) parametric space. It is seen that there is no a pronounced dependence of $W_{\|\mathrm{res}}$ on X, but there is a dependence on $|B_X|$. A scatterplot of $W_{\|\mathrm{res}}$ versus $|B_X|$ (see Figure 10b) also demonstrates a tendency of the $W_{\|\mathrm{res}}$ increase with the $|B_X|$. Indeed, the median values of $W_{\|\mathrm{res}}$ calculated within $|B_X| \leq 10$ nT, 10 nT $< |B_X| \leq 30$ nT, and $|B_X| > 30$ nT bins are 3.4, 18.4, and 49.9 keV, respectively. This implies that farther from the neutral plane the quasi-parallel whistler waves efficiently interact with more energetic electrons than closer to the neutral plane. If these whistler waves are capable to scatter electrons into the loss cone, one may expect that electrons with higher energies will precipitate at higher latitudes, at least, in the beginning of the prolonged dipolarizations. Supposing parallel propagation, when waves and resonant particles move in opposite directions, and under assumption that the waves propagating from the equator have larger amplitudes, particles interacting with the waves well outside the equatorial plane should mainly precipitate in the hemisphere opposite to that of resonant interaction.

5. Conclusions

In the present paper, we have determined for the first time the characteristic of resonant electrons interacting with the quasi-parallel whistler waves during ∼13 min following the onset of the prolonged dipolarizations when multiple B_Z pulses or DFBs were observed. During such intervals MMS observations in burst mode were available. These observations make it possible to calculate the growth rate γ of whistler waves on the time scale of their bursts (approximately a few seconds). We have found that in the majority of events from our data base electrons with energies $W_{\mathrm{res}} \geq 10$ keV and pitch angles $\alpha_{\mathrm{res}} \sim 100°–130°$ and $\alpha_{\mathrm{res}} \sim 50°–80°$ make the major positive contribution to the growth rate of these waves. The large values of W_{res} were due to the low frequencies of the observed whistler waves $f_w \leq 0.2 f_{\mathrm{ce}}$ and large values of the local f_{ce}.

The large values of W_{res} explain the unexpected values of $T_\perp / T_\| < 1.0$ observed during many whistler bursts from our data base. Because of the proximity of energies of resonant electrons to the high-energy threshold of FPI instrument, the corresponding values of $T_\perp / T_\|$ do not represent correctly the real anisotropy of the electron population responsible for the whistler wave generation. Thus, we suggest that the whistlers observed during periods when $T_\perp / T_\| < 1.0$ may still have been generated locally due to the cyclotron instability as whistler waves observed during periods with clear perpendicular electron anisotropy.

We show that low-frequency quasi-parallel whistler waves can scatter electrons into the loss cone. In the majority of events from our data base, the resonant electrons which can potentially be scattered into the loss cone during ∼13 min following the dipolarization onset have energies ∼10–20 keV.

We have revealed that during the prolonged dipolarizations whistler waves play an important role in dynamics of electron velocity distribution function observed by FPI instrument in the energy range ≥2 keV. In this energy range, the resonant electrons of lower energies transfer the energy to the waves, which, in turn, transfer their energy to the resonant electrons of higher energy. Thus, being excited due to cyclotron instability driven by temperature anisotropy of electron distribution function in the energy range ≥2 keV, whistler waves play an important role in energy exchange between the lower and higher energy parts of suprathermal electron distribution. This may lead to the transformation of this distribution from Maxwellian to a power law shape.

Data Availability Statement

The authors thank the MMS Data Center (https://lasp.colorado.edu/mms/sdc/public/) from which the data used in this paper were obtained. For data analysis we also used SPEDAS 4.1 software.

Acknowledgments
E. V. Panov acknowledges the Austrian Science Fund (FWF) I 3506-N27. The French LPP involvement for the SCM instrument is supported by CNES and CNRS.

References

Akilov, G. P., & Kantorovich, L. V. (1982). *Functional analysis* (2nd ed.). Elsevier. Pergamon Press.
Baumjohann, W., Hesse, M., Kokubun, S., Mukai, T., Nagai, T., & Petrukovich, A. A. (1999). Substorm dipolarization and recovery. *Journal of Geophysical Research*, *104*, 24995–25000. https://doi.org/10.1029/1999JA900282
Birn, J., Liu, J., Runov, A., Kepko, L., & Angelopoulos, V. (2019). On the contribution of dipolarizing flux bundles to the substorm current wedge and to flux and energy transport. *Journal of Geophysical Research: Space Physics*, *124*, 5408–5420. https://doi.org/10.1029/2019JA026658
Birn, J., Merkin, V. G., Sitnov, M. I., & Otto, A. (2018). MHD stability of magnetotail configurations with a B_z hump. *Journal of Geophysical Research: Space Physics*, *123*, 3477–3492. https://doi.org/10.1029/2018JA025290
Birn, J., Runov, A., & Hesse, M. (2014). Energetic electrons in dipolarization events: Spatial properties and anisotropy. *Journal of Geophysical Research: Space Physics*, *119*, 3604–3616. https://doi.org/10.1002/2013JA019738
Breuillard, H., Le Contel, O., Retino, A., Chasapis, A., Chust, T., Mirioni, L., et al. (2016). Multi spacecraft analysis of dipolarization fronts and associated whistler wave emissions using MMS data. *Geophysical Research Letters*, *43*, 7279–7286. https://doi.org/10.1002/2016gl069188
Burch, J. L., Moore, T. E., Torbert, R. B., & Giles, B. L. (2016). Magnetospheric Multiscale overview and science objectives. *Space Science Reviews*, *199*(1–4), 5–21. https://doi.org/10.1007/s11214-015-0164-9
Delcourt, D. C. (2002). Particle acceleration by inductive electric fields in the inner magnetosphere. *Journal of Atmospheric and Solar-Terrestrial Physics*, *64*, 551–559. https://doi.org/10.1016/s1364-6826(02)00012-3
Delcourt, D. C., & Sauvaud, J. A. (1994). Plasma sheet ion energization during dipolarization events. *Journal of Geophysical Research*, *99*, 97–108. https://doi.org/10.1029/93JA01895
Fu, H. S., Cao, J. B., Cully, C. M., Khotyaintsev, Y. V., Vaivads, A., Angelopoulos, V., et al. (2014). Whistler-mode waves inside flux pileup region: Structured or unstructured? *Journal of Geophysical Research: Space Physics*, *119*, 9089–9100. https://doi.org/10.1002/2014ja020204
Fu, H. S., Khotyaintsev, Y. V., André, M., & Vaivads, A. (2011). Fermi and betatron acceleration of suprathermal electrons behind dipolarization fronts. *Geophysical Research Letters*, *38*, L16104. https://doi.org/10.1029/2011GL048528
Fu, H. S., Khotyaintsev, Y. V., Vaivads, A., André, M., Sergeev, V. A., Huang, S. Y., et al. (2012). Pitch angle distribution of suprathermal electrons behind dipolarization fronts: A statistical overview. *Journal of Geophysical Research*, *117*, A12221. https://doi.org/10.1029/2012JA018141
Gabrielse, C., Harris, C., Angelopoulos, V., Artemyev, A., & Runov, A. (2016). The role of localized inductive electric fields in electron injections around dipolarizing flux bundles. *Journal of Geophysical Research: Space Physics*, *121*, 9560–9585. https://doi.org/10.1002/2016ja023061
Grigorenko, E. E., Dubyagin, S., Malykhin, A. Y., Khotyaintsev, Y. V., Kronberg, E. A., Lavraud, B., & Ganushkina, N. Y. (2018). Intense current structures observed at electron kinetic scales in the near-Earth magnetotail during dipolarization and substorm current wedge formation. *Geophysical Research Letters*, *45*, 602–611. https://doi.org/10.1002/2017GL076303
Grigorenko, E. E., Kronberg, E. A., Daly, P. W., Ganushkina, N. Y., Lavraud, B., Sauvaud, J.-A., & Zelenyi, L. M. (2016). Origin of low proton-to-electron temperature ratio in the Earth's plasma sheet. *Journal of Geophysical Research-A: Space Physics*, *121*, 9985–10004. https://doi.org/10.1002/2016JA022874
Grigorenko, E. E., Malykhin, A. Y., Shklyar, D. R., Fadanelli, S., Lavraud, B., Panov, E. V., et al. (2020). Investigation of electron distribution functions associated with whistler waves at dipolarization fronts in the Earth's magnetotail: MMS observations. *Journal of Geophysical Research: Space Physics*, *125*, e2020JA028268. https://doi.org/10.1029/2020JA028268
Gurnett, D. A., Frank, L. A., & Lepping, R. P. (1976). Plasma waves in the distant magnetotail. *Journal of Geophysical Research*, *81*(34), 6059–6071. https://doi.org/10.1029/JA081i034p06059
Helliwell, R. A. (1965). *Whistlers and related ionospheric phenomena*. Stanford University Press.
Huang, S. Y., Zhou, M., Deng, X. H., Yuan, Z. G., Pang, Y., Wei, Q., et al. (2012). Kinetic structure and wave properties associated with sharp dipolarization front observed by Cluster. *Annales de Geophysique*, *30*(1), 97–107. https://doi.org/10.5194/angeo-30-97-2012
Karpman, V. I., Istomin, J. N., & Shklyar, D. R. (1974). Nonlinear theory of quasi-monochromatic whistle-mode packet in inhomogeneous plasma. *Plasma Physics*, *16*, 685–703. https://doi.org/10.1088/0032-1028/16/8/001
Khotyaintsev, Y. V., Cully, C. M., Vaivads, A., André, M., & Owen, C. J. (2011). Plasma jet braking: Energy dissipation and nonadiabatic electrons. *Physical Review Letters*, *106*(16), 165001. https://doi.org/10.1103/PhysRevLett.106.165001
Le Contel, O., Leroy, P., Roux, A., Coillot, C., Alison, D., Bouabdellah, A., et al. (2016). The search-coil magnetometer for MMS. *Space Science Reviews*, *199*(1–4), 257–282. https://doi.org/10.1007/s11214-014-0096-9
Le Contel, O., Roux, A., Jacquey, C., Robert, P., Berthomier, M., Chust, T., et al. (2009). Quasi-parallel whistler mode waves observed by THEMIS during near-Earth dipolarizations. *Annales de Geophysique*, *27*(6), 2259–2275. https://doi.org/10.5194/angeo-27-2259-2009

Liang, J., Ni, B., Cully, C. M., Donovan, E. F., Thorne, R. M., & Angelopoulos, V. (2012). Electromagnetic ELF wave intensification with fast earthward flows in mid-tail plasma sheet. *Annales de Geophysique*, *30*(3), 467–488. https://doi.org/10.5194/angeo-30-467-2012

Liu, J., Angelopoulos, V., Runov, A., & Zhou, X.-Z. (2013). On the current sheets surrounding dipolarizing flux bundles in the magnetotail. The case of wedgelets. *Journal of Geophysical Research*, *118*, 2000–2020. https://doi.org/10.1002/jgra.50092

Liu, J., Angelopoulos, V., Runov, A., & Zhou, X.-Z. (2014). Magnetic flux transport by dipolarizing flux bundles. *Journal of Geophysical Research: Space Physics*, *119*, 909–926. https://doi.org/10.1002/2013JA019395

Lui, A. T. Y. (1996). Current disruption in the Earth's magnetosphere: Observations and models. *Journal of Geophysical Research*, *101*, 13067–13088. https://doi.org/10.1029/96ja00079

Lui, A. T. Y. (2004). Potential plasma instabilities for substorm expansion onsets. *Space Science Reviews*, *113*, 127–206. https://doi.org/10.1023/B:SPAC.0000042942.00362.4e10.1023/b:spac.0000042942.00362.4e

Lui, A. T. Y. (2011). Reduction of the cross-tail current during near-Earth dipolarization with multisatellite observations. *Journal of Geophysical Research*, *116*, A12239. https://doi.org/10.1029/2011JA017107

Malykhin, A. Y., Grigorenko, E. E., Kronberg, E. A., & Daly, P. W. (2018). The effect of the betatron mechanism on the dynamics of suprathermal electron fluxes within dipolarizations in the magnetotail. *Geomagnetism and Aeronomy*, *58*, 744–752. https://doi.org/10.1134/s0016793218060099

Malykhin, A. Y., Grigorenko, E. E., Kronberg, E. A., Daly, P. W., & Kozak, L. V. (2019). Acceleration of protons and heavy ions to suprathermal energies during dipolarizations in the near-Earth magnetotail. *Annales Geophysicae*, *37*, 549–559. https://doi.org/10.5194/angeo-37-549-2019

Malykhin, A. Y., Grigorenko, E. E., Kronberg, E. A., Koleva, R., Ganushkina, N. Y., Kozak, L., & Daly, P. W. (2018). Contrasting dynamics of electrons and protons in the near-Earth plasma sheet during dipolarizations. *Annales Geophysicae*, *36*, 741–760. https://doi.org/10.5194/angeo-36-741-201810.5194/angeo-36-741-2018

McPherron, R. L., Russell, C. T., & Aubry, M. A. (1973). Satellite studies of magnetospheric substorms on August 15, 1968, 9, phenomenological model for substorms. *Journal of Geophysical Research*, *78*, 3131–3149. https://doi.org/10.1029/ja078i016p03131

Means, J. D. (1972). Use of the three-dimensional covariance matrix in analyzing the polarization properties of plane waves. *Journal of Geophysical Research*, *77*(28), 5551–5559. https://doi.org/10.1029/JA077i028p05551

Merkin, V. G., Panov, E. V., Sorathia, K., & Ukhorskiy, A. Y. (2019). Contribution of bursty bulk flows to the global dipolarization of the magnetotail during an isolated substorm. *Journal of Geophysical Research: Space Physics*, *124*, 8647–8668. https://doi.org/10.1029/2019JA026872

Merkin, V. G., & Sitnov, M. I. (2016). Stability of magnetotail equilibria with a tailward B_z gradient. *Journal of Geophysical Research*, *121*, 9411–9426. https://doi.org/10.1002/2016JA023005

Miura, A., Ohtani, S., & Tamao, T. (1989). Ballooning instability and structure of diamagnetic hydromagnetic waves in a model magnetosphere. *Journal of Geophysical Research*, *94*(A11), 15231–15242. https://doi.org/10.1029/JA094iA11p15231

Nakamura, R., Retinò, A., Baumjohann, W., Volwerk, M., Erkaev, N., Klecker, B., et al. (2009). Evolution of dipolarization in the near-Earth current sheet induced by Earthward rapid flux transport. *Annales Geophysicae*, *27*, 1743–1754. https://doi.org/10.5194/angeo-27-1743-200910.5194/angeo-27-1743-2009

Nakamura, R., Varsani, A., Genestreti, K. J., Le Contel, O., Nakamura, T., Baumjohann, W., et al. (2018). Multiscale currents observed by MMS in the flow braking region. *Journal of Geophysical Research: Space Physics*, *123*, 1260–1278. https://doi.org/10.1002/2017JA024686

Nosé, M., Lui, A. T. Y., Ohtani, S., Mauk, B. H., McEntire, R. W., Williams, D. J., et al. (2000). Acceleration of oxygen ions of ionospheric origin in the near-Earth magnetotail during substorms. *Journal of Geophysical Research*, *105*, 7669–7677. https://doi.org/10.1029/1999JA000318

Ohtani, S., Shay, M. A., & Mukai, T. (2004). Temporal structure of the fast convective flow in the plasma sheet: Comparison between observations and two-fluid simulations. *Journal of Geophysical Research*, *109*, A03210. https://doi.org/10.1029/2003JA010002

Panov, E. V., Baumjohann, W., Nakamura, R., Pritchett, P. L., Weygand, J. M., & Kubyshkina, M. V. (2019a). Ionospheric footprints of detached magnetotail interchange heads. *Geophysical Research Letters*, *46*, 7237–7247. https://doi.org/10.1029/2019GL083070

Panov, E. V., Baumjohann, W., Nakamura, R., Weygand, J. M., Giles, B. L., Russell, C. T., et al. (2019b). Continent-wide R1/R2 current system and ohmic losses by broad dipolarization-injection fronts. *Journal of Geophysical Research: Space Physics*, *124*, 4064–4082. https://doi.org/10.1029/2019JA026521

Panov, E. V., Lu, S., & Pritchett, P. L. (2020). Understanding spacecraft trajectories through detached magnetotail interchange heads. *Journal of Geophysical Research: Space Physics*, *125*, e2020JA027930. https://doi.org/10.1029/2020JA027930

Pollock, C., Moore, T., Jacques, A., Burch, J., Gliese, U., Saito, Y., et al. (2016). Fast Plasma Investigation for Magnetospheric Multiscale. *Space Science Reviews*, *199*(1–4), 331–406. https://doi.org/10.1007/s11214-016-0245-4

Pritchett, P. L. (2015). Instability of current sheets with a localized accumulation of magnetic flux. *Physics of Plasmas*, *22*(6), 062102. https://doi.org/10.1063/1.4921666

Pritchett, P. L., & Coroniti, F. V. (2011). Plasma sheet disruption by interchange-generated flow intrusions. *Geophysical Research Letters*, *38*, L10102. https://doi.org/10.1029/2011GL047527

Pritchett, P. L., Coroniti, F. V., & Nishimura, Y. (2014). The kinetic ballooning/interchange instability as a source of dipolarization fronts and auroral streamers. *Journal of Geophysical Research: Space Physics*, *119*, 4723–4739. https://doi.org/10.1002/2014JA019890

Roux, A., Perraut, S., Rpbert, P., Morane, A., Pedersen, A., Korth, A., et al. (1991). Plasma sheet instability related to the westward traveling surge. *Journal of Geophysical Research*, *96*(A10), 17697–17714. https://doi.org/10.1029/91JA01106

Runov, A., Angelopoulos, V., Zhou, X. -Z., Zhang, X. -J., Li, S., Plaschke, F., & Bonnell, J. (2011). A THEMIS multicase study of dipolarization fronts in the magnetotail plasma sheet. *Journal of Geophysical Research*, *116*, A05216. https://doi.org/10.1029/2010JA016316

Russell, C. T., Anderson, B. J., Baumjohann, W., Bromund, K. R., Dearborn, D., Fischer, D., et al. (2016). The Magnetospheric Multiscale magnetometers. *Space Science Reviews*, *199*(1–4), 189–256. https://doi.org/10.1007/s11214-014-0057-3

Sagdeev, R. Z., & Shafranov, V. D. (1961). On the instability of a plasma with anisotropic distribution of velocities in a magnetic field. *Soviet Physics–JETP*, *12*(1), 130–132.

Samson, J. C., & Olson, J. V. (1980). Some comments on the description of the polarization states of waves. *Geophysical Journal of the Royal Astronomical Society*, *61*, 115–129. https://doi.org/10.1111/j.1365-246x.1980.tb04308.x

Schmid, D., Nakamura, R., Plaschke, F., Volwerk, M., & Baumjohann, W. (2015). Two states of magnetotail dipolarization fronts: A statistical studies. *Journal of Geophysical Research: Space Physics*, *120*, 1096–1108. https://doi.org/10.1002/2014JA020380

Sergeev, V. A., Angelopoulos, V., & Nakamura, R. (2012). Recent advances in understanding substorm dynamics. *Geophysical Research Letters*, *39*, L05101. https://doi.org/10.1029/2012GL050859

Shiokawa, K., Miyashita, Y., Sinohara, I., & Matsuoka, A. (2005). Decrease in B_Z prior to the dipolarization in the near-Earth plasma sheet. *Journal of Geophysical Research*, *110*, A09219. https://doi.org/10.1029/2005JA011144

Shklyar, D., & Matsumoto, H. (2009). Oblique whistler-mode waves in the inhomogeneous magnetospheric plasma: Resonant interactions with energetic charged particles. *Surveys in Geophysics*, *30*(2), 55–104. https://doi.org/10.1007/s10712-009-9061-7

Shklyar, D. R. (2011). Wave-particle interactions in marginally unstable plasma as a means of energy transfer between energetic particle populations. *Physics Letters*, *375*(14), 1583–1587. https://doi.org/10.1016/j.physleta.2011.02.067

Shklyar, D. R. (2017). Energy transfer from lower energy to higher-energy electrons mediated by whistler waves in the radiation belts. *Journal of Geophysical Research: Space Physics*, *122*, 640–655. https://doi.org/10.1002/2016JA023263

Smets, R., Delcourt, D., Sauvaud, J.-A., & Koperski, P. (1999). Electron pitch angle distributions following a dipolarization phase of a substorm: Interball-tail observations and modeling. *Journal of Geophysical Research*, *104*(A7), 14571–14581. https://doi.org/10.1029/1998JA900162

Takada, T., Nakamura, R., Baumjohann, W., Asano, Y., Volwerk, M., Zhang, T. L., et al. (2006). Do BBFs contribute to inner magnetosphere dipolarizations: Concurrent Cluster and Double Star observations. *Geophysical Research Letters*, *33*, L21109. https://doi.org/10.1029/2006GL027440

Tenerani, A., Le Contel, O., Califano, F., Robert, P., Fontaine, D., Cornilleau-Wehrlin, N., & Sauvaud, J.-A. (2013). Cluster observations of whistler waves correlated with ion-scale magnetic structures during the 17 August 2003 substorm event. *Journal of Geophysical Research: Space Physics*, *118*, 6072–6089. https://doi.org/10.1002/jgra.50562

Viberg, H., Khotyaintsev, Y. V., Vaivads, A., André, M., Fu, H. S., & Cornilleau-Wehrlin, N. (2014). Whistler mode waves at magnetotail dipolarization fronts. *Journal of Geophysical Research: Space Physics*, *119*, 2605–2611. https://doi.org/10.1002/2014JA019892

Wu, P., Fritz, T. A., Larvaud, B., & Lucek, E. (2006). Substorm associated magnetotail energetic electrons pitch-angle evolutions and flow reversals: Cluster observation. *Geophysical Research Letters*, *33*, L17101. https://doi.org/10.1029/2006GL026595

Zhang, X., Angelopoulos, V., Artemyev, A. V., & Liu, J. (2019). Energy transport by whistler waves around dipolarizing flux bundles. *Geophysical Research Letters*, *46*, 11718–11727. https://doi.org/10.1029/2019GL084226

Zhang, X.-J., & Angelopoulos, V. (2014). On the relationship of electrostatic cyclotron harmonic emissions with electron injections and dipolarization fronts. *Journal of Geophysical Research: Space Physics*, *119*, 2536–2549. https://doi.org/10.1002/2013JA019540

Zhang, Y., Matsumoto, H., & Kojima, H. (1999). Whistler mode waves in the magnetotail. *Journal of Geophysical Research*, *104*, 28633–28644. https://doi.org/10.1029/1999JA900301

Zhao, M. J., Fu, H. S., Liu, C. M., Chen, Z. Z., Xu, Y., Giles, B. L., & Burch, J. L. (2019). Energy range of electron rolling pin distribution behind dipolarization front. *Geophysical Research Letters*, *46*, 2390–2398. https://doi.org/10.1029/2019GL082100